AIAA JOURNAL
Vol. 46, No. 12, December 2008

Evaluation of Two High-Order Weighted Essentially Nonoscillatory Schemes

Robert H. Nichols*
University of Alabama at Birmingham, Birmingham, Alabama 35294
Robert W. Tramel†
Digital Fusion, Inc., Huntsville, Alabama 35806
and
Pieter G. Buning‡
NASA Langley Research Center, Hampton, Virginia 23681

DOI: 10.2514/1.36849

Two fifth-order spatial weighted essentially nonoscillatory schemes for the convective terms were added to the OVERFLOW 2 implicit overset Navier–Stokes flow solver. The method used to incorporate the schemes is similar to a monotone upstream-centered scheme for conservation laws and requires no modification of the viscous terms, transport equations, or turbulence models in the code. The new flux calculation schemes were applied to problems involving vortex convection, strong shocks, and large scale unsteady flows. The weighted essentially nonoscillatory schemes were found to have much lower numerical dissipation/dispersion than traditional third-order spatial monotone upstream-centered schemes for conservation laws. Both weighted essentially nonoscillatory schemes were numerically robust over a wide range of Mach numbers when solved using the existing implicit schemes within OVERFLOW 2. The weighted essentially nonoscillatory schemes also provided improved numerical accuracy over traditional third-order spatial monotone upstream-centered schemes for conservation laws on the same computational grid for all the applications examined here. The weighted essentially nonoscillatory schemes are 10–30% more expensive than the third-order spatial monotone upstream-centered schemes for conservation laws depending on choice of implicit solver.

Nomenclature

a	=	coefficients in a series expansion
b	=	wing semispan
Ch	=	wing chord
C_{b1}	=	Spalart–Allmaras turbulence model constant
C_{vor}	=	rotational flow correction constant
c	=	speed of sound
$\hat{c}$	=	Roe averaged speed of sound
D	=	diameter
dt	=	computational time step
E	=	total internal energy
F	=	flux vector
g	=	WENOM mapped weights
H_0	=	total enthalpy
h	=	approximation function for conserved variable
L	=	length
P	=	turbulent production
p	=	pressure
Q	=	conserved variable vector
q	=	variable to be extrapolated
$\hat{q}$	=	extrapolated approximation of variable
$\bar{R}$	=	radius
S	=	wave speed
S_t	=	strain magnitude
U	=	velocity
$\hat{U}$	=	Roe averaged velocity
w	=	modified weights for WENO
x, y, z	=	spatial directions
β	=	smoothness indicator for WENO
Γ	=	vortex strength
γ	=	optimal weights for WENO and WENOM
$\Delta x, \Delta y, \Delta z$	=	spatial direction increments
ε	=	small number
θ	=	angular location in degrees
$\tilde{\nu}$	=	Spalart–Allmaras turbulence variable
ρ	=	density
Ω	=	vorticity magnitude
ω	=	local vorticity

Subscripts

i	=	spatial index
k	=	counter index for WENO and WENOM weights
L	=	left state
R	=	right state

Superscripts

Ref	=	reference value
0	=	vortex center location
*	=	intermediate state
∞	=	freestream value

Presented as Paper 3920 at the Applied Aerodynamics Conference, Miami, FL, 21–25 July 2007; received 25 January 2008; revision received 29 July 2008; accepted for publication 29 July 2008.

*Research Associate Professor, Department of Mechanical Engineering. Member AIAA.
†Staff Engineer/Scientist. Senior Member AIAA.
‡Aerospace Engineer, Configuration Aerodynamics Branch, Mail Stop 499. Associate Fellow AIAA.

Introduction

HIGHER order numerical schemes offer two principal advantages over lower order schemes. Higher order schemes can provide more accurate solutions using fewer grid points for both steady and unsteady flow solutions. Higher order schemes also provide much lower numerical dissipation for unsteady flow applications. The lower numerical dissipation allows small disturbances to propagate over large distances. This is critical to

several application areas including tip vortex tracking, large eddy simulation (LES), high angle-of-attack flight, and acoustics. Current efforts at modeling these unsteady problems with state-of-the-art second- and third-order spatial algorithms require extremely fine grids to minimize the numerical dissipation and dispersion. For instance, if the grid spacing in a computational simulation were reduced by a factor of 2, then for a fifth-order scheme the numerical error should be reduced by a factor proportional to 2^5. To reduce numerical errors to a comparable level using a second-order scheme would require a corresponding reduction in grid spacing of $2^{(5-2)} = 8$. In three dimensions these estimates would dictate that a factor of $8^3 = 512$ times finer grid would be required. Considerations such as this clearly demonstrate the potential advantages inherent in the use of higher order schemes.

Higher order compact difference schemes [1–3] have been applied to simple geometries and have been useful in developing a theoretical understanding of these complex flows, but these algorithms are only rarely applied to full aircraft-type geometries [4] because of the difficulties in grid generation and solver numerical stability. The grid metrics and volumes used in finite difference codes must be compatible with the differencing scheme used for the viscous and inviscid fluxes within the code or the resulting algorithm will not satisfy the geometric conservation law property of [5]. If compact differences are used to obtain higher order accuracy for the inviscid fluxes, then the grid metrics and volumes must also be evaluated with higher order accurate compact differences. All of the numerical differences appearing in the viscous terms, species equations, and turbulent transport equations must also be performed with higher order accurate compact differencing to be compatible with the grid metrics and volumes. All boundaries must also include the appropriate higher order compact formulation or the order of the scheme will be degraded. Overset flow solvers must also include special logic to change the numerical stencil at hole boundaries (points removed from the active computational domain) to assure that only valid field and fringe points are included in the flux reconstruction. Thus it is not a trivial exercise to add higher order compact differencing to an existing code. In addition, central difference compact schemes have very little built in numerical dissipation and as such are unsuited for use on problems with discontinuities without the addition of ad hoc smoothing or filtering schemes which have to be tuned by hand for each new application of the scheme.

Higher order inviscid fluxes can also be obtained by using finite difference versions of essentially nonoscillatory (ENO) [6] and weighted essentially nonoscillatory (WENO) [7,8] algorithms. In the ENO approach, uniformly higher order accuracy is achieved by using several different upwind biased candidate stencils of the desired order of accuracy, whereas the nonoscillatory nature of the scheme is ensured by selecting the single stencil for which the interpolating polynomial reconstructed from the nodal values is smoothest in some appropriate sense. In this manner the method avoids interpolating across discontinuities and the resulting overshoots and oscillations which typically result when using higher order schemes in the presence of discontinuities. Thus, the ENO scheme is highly nonlinear and data dependent. The next advance in this line of algorithms came with the development of the WENO family of numerical schemes. Liu et al. [7] observed that a convex combination of all of the rth order candidate stencils used in the ENO scheme can be used to create an $(r+1)$ order WENO scheme. Smoothness indicators are used to set to zero the weight of any stencil that contains a discontinuity. Jiang and Shu [8] developed a set of optimal weights such that a $(2r-1)$th order scheme could be constructed. The ENO and WENO schemes are both robust and accurate. When ENO and WENO schemes are used to solve systems of equations both methods make use of upwinding in characteristic fields and require a large number of projections (equal to the width of the total stencil) onto the left and right eigenvectors of the flux Jacobians at each grid half-node. These schemes require substantially more floating point operations to construct the numerical flux functions than their more traditional counterparts.

In this work the WENO methodology is used to increase the spatial order of variable extrapolation to the grid half-nodes with an upwind flux reconstruction algorithm in a form analogous to monotone upstream-centered schemes for conservation laws (MUSCL) [9]. The final inviscid flux contribution to the residual is calculated from the central difference of the reconstructed flux at the half-nodes, so second-order central difference grid metrics and volumes are compatible with this approach and sufficient to ensure that geometric conservation is preserved. The approach adopted in this work can easily be added to any finite difference flow solver that makes use of the MUSCL framework without the need for extensive code modifications.

In this study it is assumed that second-order terms are sufficient to accurately capture the viscous term contribution. This may not be the case for all flows and is left for a topic of future study. De Rango and Zingg [10] demonstrated that using lower order convective flux formulations for transport-type turbulence models does not affect the accuracy of the flow solver when higher order methods are used for the inviscid fluxes. Hence the transport turbulence models in the code were not modified in this study. An option to use the fifth-order WENO schemes for the convection terms of the species equations was added to the code. All boundary conditions with the exception of interpolated boundaries, overlap boundaries, and symmetry planes are treated using the existing first-order approximations. The primary goal of this effort is to develop a robust and accurate low numerical dissipation algorithm that can be used in conjunction with complex geometries and existing hybrid Reynolds averaged Navier–Stokes/large eddy simulation (hybrid RANS/LES) turbulence models for unsteady flow simulations.

Theory

HLLC Scheme

Nichols et al. [11] recently incorporated a Harten, Lax, and van Leer contact (HLLC) [12] inviscid flux scheme into the OVERFLOW 2 structured grid overset flow solver. The HLLC [12] scheme is an approximate Riemann solver based on the HLL [13] methodology. The HLL methodology divides the Riemann fan into four regions separated by the fastest left (S_L) and right (S_R) running waves and a contact discontinuity (S_M) as shown in Fig. 1. The resulting numerical flux is given by

$$F_{LR}^{\mathrm{HLLC}} = \begin{cases} F_L & \text{if } S_L > 0 \\ F_L^* & \text{if } S_L \le 0 \le S_M \\ F_R^* & \text{if } S_M \le 0 \le S_R \\ F_R & \text{if } S_R < 0 \end{cases} \tag{1}$$

Here F is the flux at a given face for one-dimensional flow by

$$F = \begin{bmatrix} \rho U \\ \rho U^2 + p \\ \rho U H_0 - p \end{bmatrix} \tag{2}$$

The left (F_L) and right (F_R) fluxes are based on the left (Q_L) and right (Q_R) state variables. The intermediate state variables (denoted by *) are obtained from the Rankine–Hugonoit relations [14]

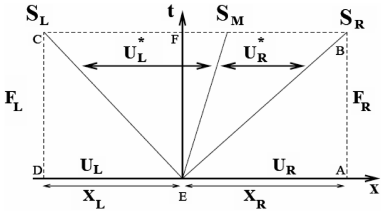

Fig. 1 Simplified Riemann fan for the HLLC scheme.

$$Q_L^* = \begin{bmatrix} \rho_L^* \\ (\rho U)_L^* \\ (\rho E)_L^* \end{bmatrix} = \frac{1}{S_L - S_M} \begin{bmatrix} (S_L - U_L)\rho_L \\ (S_L - U_L)(\rho U)_L + (p^* - p_L) \\ (S_L - U_L)(\rho E)_L - p_L U_L + p^* S_M \end{bmatrix} \tag{3}$$

$$Q_R^* = \begin{bmatrix} \rho_R^* \\ (\rho U)_R^* \\ (\rho E)_R^* \end{bmatrix} = \frac{1}{S_R - S_M} \begin{bmatrix} (S_R - U_R)\rho_R \\ (S_R - U_R)(\rho U)_R + (p^* - p_R) \\ (S_R - U_R)(\rho E)_R - p_R U_R + p^* S_M \end{bmatrix} \tag{4}$$

The resulting intermediate fluxes are given by

$$F_L^* \equiv F(Q_L^*) = \begin{bmatrix} S_M \rho_L^* \\ S_M(\rho U)_L^* + p^* \\ S_M((\rho E)_L^* + p^*) \end{bmatrix} \tag{5}$$

$$F_R^* \equiv F(Q_R^*) = \begin{bmatrix} S_M \rho_R^* \\ S_M(\rho U)_R^* + p^* \\ S_M((\rho E)_R^* + p^*) \end{bmatrix} \tag{6}$$

where

$$\begin{aligned} p^* &= \rho_L(U_L - S_L)(U_L - S_M) + p_L \\ &= \rho_R(U_R - S_R)(U_R - S_M) + p_R \end{aligned} \tag{7}$$

The intermediate signal velocity (see Fig. 1) is given by

$$S_M = \frac{\rho_R U_R(S_R - U_R) - \rho_L U_L(S_L - U_L) + p_L - p_R}{\rho_R(S_R - U_R) - \rho_L(S_L - U_L)} \tag{8}$$

The signal velocities S_L and S_R (see Fig. 1) are defined based on Roe averaged quantities following Einfeldt [15]

$$S_L = \min(U_L - c_L, \hat{U}_L - \hat{c}_L) \tag{9}$$

$$S_R = \min(U_R - c_R, \hat{U}_R - \hat{c}_R) \tag{10}$$

The flux difference at node i is then given by $F_i - F_{i-1}$. The HLLC scheme has many nice features including the following:

1) exact preservation of isolated shock, contact, and shear waves;
2) positivity preserving for scalar quantities;
3) enforcement of the entropy condition;
4) no detailed knowledge of the eigenstructure of the flux-Jacobian matrices required for flux reconstruction;
5) easily extendable to any passively advected scalar.

The conserved variables $(\rho, \rho u, \rho v, \rho w, \rho e_0)$ are stored at the nodes (i) in OVERFLOW 2. The HLLC scheme requires flow variable information at the half-nodes $(i - 1/2, i + 1/2)$ to construct the contribution of the inviscid fluxes to the residual. The half-node information is currently obtained using a MUSCL interpolation scheme. The primitive variables (p, u, v, w, T) at the nodes are interpolated to the half-node using the MUSCL scheme to obtain first-, second-, or third-order spatial approximations of the primitive variables. OVERFLOW 2 currently has three flux limiter choices to suppress spurious oscillations during the solution process.

WENO

Interpolating flow variables using a fifth-order spatial WENO [16] rather than a third-order spatial MUSCL scheme provides a relatively inexpensive means to achieve a higher order numerical capability for the inviscid fluxes. Here the primitive variables (p, u, v, w, T) are interpolated to the grid half-nodes using the WENO scheme. The weighting in the WENO scheme serves to provide limiting to suppress spurious oscillations during the solution process. Using the WENO scheme in this way avoids expensive projections onto characteristic states associated with most WENO formulations. A somewhat similar approach has been developed by Shen et al. [17] in conjunction with a Roe flux difference scheme.

The formulation of the WENO interpolation used in this study follows that of Henrick et al. [18] and Merriman [19]. The WENO methodology views the fifth-order approximation of a function as being built from a convex combination of three third-order approximations as shown in Fig. 2. The fifth-order left and right interpolated variables are then written as

$$\hat{q}^{\,L}_{i+\frac{1}{2}} = w_0^L \hat{q}^{L0}_{i+\frac{1}{2}} + w_1^L \hat{q}^{L1}_{i+\frac{1}{2}} + w_2^L \hat{q}^{L2}_{i+\frac{1}{2}} \tag{11}$$

$$\hat{q}^{\,R}_{i+\frac{1}{2}} = w_0^R \hat{q}^{R0}_{i+\frac{1}{2}} + w_1^R \hat{q}^{R1}_{i+\frac{1}{2}} + w_2^R \hat{q}^{R2}_{i+\frac{1}{2}} \tag{12}$$

The third-order approximations are constructed from the variables at the nodes as

$$\begin{aligned} \hat{q}^{L0}_{i+\frac{1}{2}} &= \tfrac{1}{3}q_{i-2} - \tfrac{7}{6}q_{i-1} + \tfrac{11}{6}q_i \\ \hat{q}^{L1}_{i+\frac{1}{2}} &= -\tfrac{1}{6}q_{i-1} + \tfrac{5}{6}q_i + \tfrac{1}{3}q_{i+1} \\ \hat{q}^{L2}_{i+\frac{1}{2}} &= \tfrac{1}{3}q_i + \tfrac{5}{6}q_{i+1} - \tfrac{1}{6}q_{i+2} \end{aligned} \tag{13}$$

$$\begin{aligned} \hat{q}^{R0}_{i+\frac{1}{2}} &= \tfrac{1}{3}q_{i+3} - \tfrac{7}{6}q_{i+2} + \tfrac{11}{6}q_{i+1} \\ \hat{q}^{R1}_{i+\frac{1}{2}} &= -\tfrac{1}{6}q_{i+2} + \tfrac{5}{6}q_{i+1} + \tfrac{1}{3}q_i \\ \hat{q}^{R2}_{i+\frac{1}{2}} &= \tfrac{1}{3}q_{i+1} + \tfrac{5}{6}q_i - \tfrac{1}{6}q_{i-1} \end{aligned} \tag{14}$$

For relatively smooth regions of the flow the normalized modified weights (w_k) should return to the optimal weight values (γ_k). The optimal weights γ_0, γ_1, and γ_2 for fifth-order in space are given as 0.1, 0.6, and 0.3, respectively. The optimal values yield a true fifth-order algorithm with low numerical dissipation, so it is desirable that the modified weights approach the optimal values except in regions of large discontinuities. Deviations from the ideal values cause the numerical dissipation to increase to provide numerical stability. The normalized modified weights are constructed using smoothness indicators β_k such that weights from those stencils with large variations are minimized, whereas weights from stencils in smooth regions approach the optimal values (γ_k). The smoothness indicators for the left and right states are given by [7]

$$\begin{aligned} \beta_0^L &= \frac{13}{12}(q_{i-2} - 2q_{i-1} + q_i)^2 + \frac{1}{4}(q_{i-2} - 4q_{i-1} + 3q_i)^2 \\ \beta_1^L &= \frac{13}{12}(q_{i-1} - 2q_i + q_{i+1})^2 + \frac{1}{4}(q_{i-1} - q_{i+1})^2 \\ \beta_2^L &= \frac{13}{12}(q_i - 2q_{i+1} + q_{i+2})^2 + \frac{1}{4}(3q_i - 4q_{i+1} + q_{i+2})^2 \end{aligned} \tag{15}$$

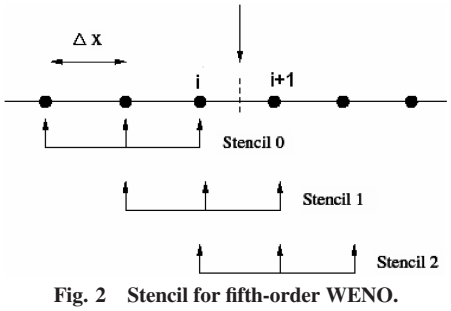

Fig. 2 Stencil for fifth-order WENO.

$$\beta_0^R = \frac{13}{12}(q_{i+3} - 2q_{i+2} + q_{i+1})^2 + \frac{1}{4}(q_{i+3} - 4q_{i+2} + 3q_{i+1})^2$$
$$\beta_1^R = \frac{13}{12}(q_{i+2} - 2q_{i+1} + q_i)^2 + \frac{1}{4}(q_{i+2} - q_i)^2$$
$$\beta_2^R = \frac{13}{12}(q_{i+1} - 2q_i + q_{i-1})^2 + \frac{1}{4}(3q_{i+1} - 4q_i + q_{i-1})^2 \tag{16}$$

The modified weights are given by

$$\tilde{w}_k = \frac{\gamma_k}{(\varepsilon + \beta_k)^2} \tag{17}$$

Here ε is a small number to avoid dividing by zero and is taken as 1.0×10^{-6} in this study. Finally the modified weights are renormalized by

$$w_k = \frac{\tilde{w}_k}{\sum_{j=0}^{2} \tilde{w}_j} \tag{18}$$

This interpolation scheme is referred to as WENO in this paper.

Mapped WENO

Recently it has been shown that the WENO scheme is only third order accurate at critical points. Henrick et al. [18] developed a mapping technique to modify the weighting near critical points to maintain fifth order everywhere. The mapped weights are given by

$$g_k = \frac{w_k(\gamma_k + \gamma_k^2 - 3\gamma_k w_k + w_k^2)}{\gamma_k^2 + w_k(1 - 2\gamma_k)} \tag{19}$$

The mapped weights are then renormalized with Eq. (18). The modified weights in Eqs. (11) and (12) are replaced with the mapped weights in this scheme. The mapped weights as a function of the modified weights for each of the ideal weights are shown in Fig. 3. The mapping causes the mapped weights (g_k) to approach the ideal weights (γ_k) for a wide range of modified weights (w_k). Thus the mapped WENO scheme maintains fifth-order accuracy for a larger region of the flow than the traditional WENO interpolation. This scheme will be referred to as WENOM.

Overset Grid Implementation of WENO and WENOM

The WENO and WENOM schemes must be modified to accommodate overset grids for implementation in OVERFLOW 2. Here we briefly review elements of the overset mesh methodology relevant to the work performed in this effort. For more information on overset mesh technology see the review article by Meakin [20] and references therein. Overset solvers divide points into three categories denoted by the value of an integer IBLANK array:

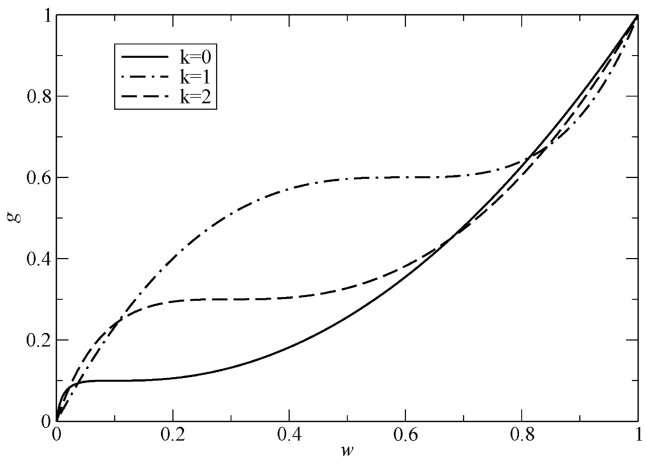

Fig. 3 Mapping function for WENO weights.

1) field points on which the flow solution is desired (IBLANK = 1);

2) hole points that lie inside of bodies and are not of interest in the solution (IBLANK = 0);

3) fringe points on which interpolated information is passed from one domain to another (IBLANK = −1).

The IBLANK array is used to exclude hole points from contributing to the solution in OVERFLOW 2 and also to prevent the implicit updating of the solution at fringe points. The WENO and WENOM schemes require a seven point stencil to create the fifth-order spatial flux. Thus three interpolation points (triple fringe) are required to support the fifth-order flux at interpolation boundaries. Traditional second- and third-order spatial methods use a five point stencil requiring two interpolation points (double fringe) at interpolation boundaries. Most existing overset flow solvers and grid assembly codes only support double fringe methods at this time. It is desirable that the WENO and WENOM algorithms degrade spatial accuracy gracefully if triple fringe boundaries are not available. To aid in this transition, functions IB2 and IB3 are defined as

$$IB2_i^L = ABS(IBLANK_{i-1} * IBLANK_i * IBLANK_{i+1})$$
$$IB3_i^L = IB2_i^L * ABS(IBLANK_{i-2} * IBLANK_{i+2}) \tag{20}$$

Equation (20) yields $IB2_i^L = 1$ if all the points are field or fringe points, and 0 if any of the points is a hole point or off the edge of the computational domain. Similarly, $IB3_i^L = 1$ if points $(i-2, i-1, i, i+1, i+2)$ are all field or fringe points, and 0 otherwise. These blanking values are incorporated into the WENO weights as

$$w_{0i}^L = w_{0i}^L * IB3_i^L$$
$$w_{1i}^L = w_{1i}^L * IB3_i^L + (1 - IB3_i^L) * IB2_i^L * r_i \tag{21}$$
$$w_{2i}^L = w_{2i}^L * IB3_i^L$$

where r_i is the van Albada [21] flux limiter. Thus the half-node approximation of the flux is fifth order if all of the $IB3_i^L$ are 1. If either or both $IB2_{i-1}^L$ and $IB2_{i+1}^L$ are 0 and $IB2_i^L$ is 1 the flux approximation drops to third order with the van Albada flux limiter. Otherwise, the flux approximation drops to first order if $IB2_i^L$ is 0. The final approximation at the half-node is then given by

$$\hat{q}^L_{i+\frac{1}{2}} = q_i + w_{0i}^L(\hat{q}^{L0}_{i+\frac{1}{2}} - q_i) + w_{1i}^L(\hat{q}^{L1}_{i+\frac{1}{2}} - q_i) + w_{2i}^L(\hat{q}^{L2}_{i+\frac{1}{2}} - q_i) \tag{22}$$

where a factor of q_i has been added in and then subtracted from each of the third-order approximations to ensure that the scheme reverts to first order in the case when all of the weights have been set to zero. The IBLANKING used for the right values is similarly done using IBLANK values from nodes $(i-1, i, i+1, i+2,$ and $i+3)$.

The grid assembly code included in OVERFLOW 2 was modified to allow triple fringe overset boundaries for both inner and outer grids. The automatic grid decomposition routines used for load balancing for parallel runs were also modified to produce triple fringe overset boundaries if the WENO or WENOM flux schemes are selected for that grid. The code currently uses second-order spatial trilinear interpolation to update overset boundary points.

Computational Cost

OVERFLOW 2 contains six different implicit solvers and seven different inviscid flux schemes. The fastest implicit solver is the diagonalized implicit solution algorithm of Pulliam and Chaussee [22]. The most robust and also the slowest implicit solver is the unfactored symmetric successive overrelaxation (SSOR) implicit algorithm of Nichols et al. [11]. The fastest inviscid flux scheme is the second-order spatial central difference scheme with scalar dissipation. The HLLC, WENO, and WENOM schemes are compared to the central difference as a measure of computational cost per time step for the fastest and slowest implicit schemes in the code in Table 1. The timings are shown for computations on a $101 \times 101 \times 101$ grid using a Pentium 4 processor with only 512 mb

Table 1 Computational cost relative to a second-order spatial central difference scheme with scalar dissipation

Implicit solution algorithm	Flux scheme	Relative cost
Diagonalized [22]	HLLC	5%
Diagonalized [22]	WENO	20%
Diagonalized [22]	WENOM	35%
SSOR [11]	HLLC	4%
SSOR [11]	WENO	12%
SSOR [11]	WENOM	19%

of cache. The additional cost of both WENO algorithms is not prohibitive for production applications. Both of the WENO algorithms were found to have similar convergence behavior and numerical stability as the third-order spatial HLLC scheme for the examples shown here.

Results

Inviscid Isentropic Vortex Convection

The ability to conserve both the vortex shape and strength is important in many unsteady cases in which a shed vortex interacts with bodies well downstream of the vortex origin. The following test case [23] can be used to examine the relative level of numerical dissipation and dispersion for inviscid flux algorithms. An isentropic vortex of nondimensional strength $\Gamma = 5$ is centered on a uniform grid of size 10 units by 10 units. Four grids will be used for most of the results presented here: 101×101 ($\Delta x = 0.1$), 81×81 ($\Delta x = 0.125$), 61×61 ($\Delta x = 0.167$), and 41×41 ($\Delta x = 0.25$). The vortex is allowed to convect downstream at a freestream Mach number of 0.5 with a nondimensional time step $[dt(U_\infty / L_{\text{Ref}})]$ of 0.01. The velocity, temperature, density, and pressure for the vortex are given by

$$
\begin{aligned}
u &= u_\infty - \frac{\Gamma}{2\pi}(z - z_0)\exp[0.5(1-\bar{R}^2)] \\
w &= \frac{\Gamma}{2\pi}(x - x_0)\exp[0.5(1-\bar{R}^2)] \\
T &= T_\infty - \frac{(\gamma-1)\Gamma^2}{8\gamma\pi}\exp(1-\bar{R}^2) \qquad \rho = T^{\frac{1}{\gamma-1}} \qquad p = \rho^\gamma
\end{aligned}
\tag{25}
$$

where $\bar{R}^2 = (x - x_0)^2 + (z - z_0)^2$ and x_0 and z_0 define the location of the vortex center at any given point in time. Here γ is the ration of specific heats. The grid is given periodic boundary conditions in the flow direction. The vortex should complete one cycle on the grid every 1000 time steps. All calculations used second-order time and three Newton subiterations. The vortex is allowed to convect through the grid 100 times. Most previous studies only allow the vortex to complete five passes through the grid, so this is a much more rigorous evaluation of the inviscid flux algorithms.

Grid size effects for uniform meshes are shown in Fig. 4. The WENOM does an excellent job of maintaining the vortex for the 101×101 and 81×81 uniform grids, and produces a good result for the 61×61 grid. The WENOM results are equivalent to the WENO results on the next finer mesh indicating that the mapping provides a less numerically dissipative scheme. The third-order results show excessive dissipation even for the 101×101 grid. Pressure contours after 100 passes through the grid are shown in Fig. 5 for the fifth-order WENOM on four levels of Cartesian grids. The vortex is preserved for the 101×101, 81×81, and 61×61 grids. The vortex cannot be found on the 41×41 grid.

The error in pressure is defined as

$$
\text{error} = \frac{|p_{\min} - p_{\min\ \text{theoretical}}|}{p_{\min\ \text{theoretical}}} \tag{26}
$$

The error is calculated after five passes through a given grid. The minimum pressure tends to oscillate slightly as the center of the vortex moves between nodes as it is convected downstream. The minimum pressure is averaged over the last 100 time steps to remove this oscillation. The error can be used to asses the spatial order of the flux algorithms used in this study. The results for all three algorithms are shown in Fig. 6. The slope of the HLLC curve in Fig. 6 indicates that algorithm is approximately third order in space. The WENO and WENOM curves both indicate that the algorithms are of approximately fifth order in space. The absolute error of the WENOM algorithm is less than that of the WENO algorithm for the same grid.

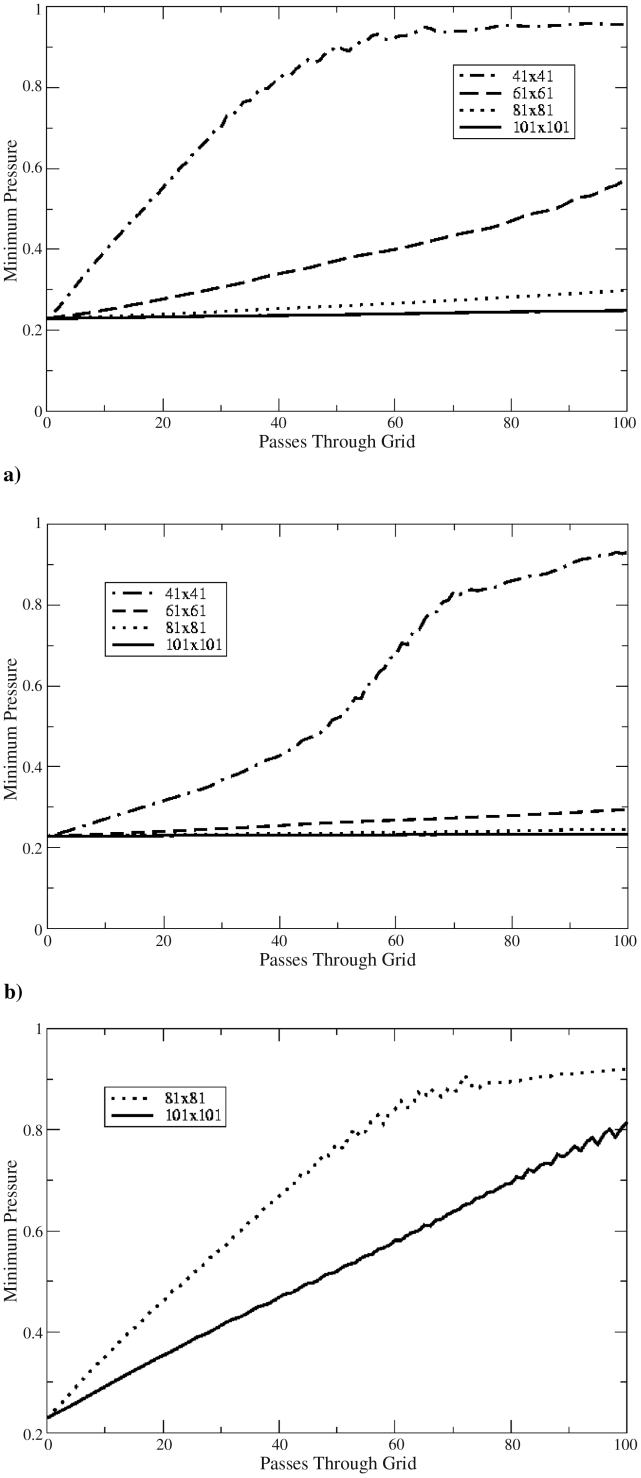

Fig. 4 a) Effect of grid size on the minimum pressure for the convecting vortex using the fifth-order HLLC with WENO. b) Effect of grid size on the minimum pressure for the convecting vortex using fifth-order HLLC with WENOM. c) Effect of grid size on the minimum pressure for the convecting vortex using third-order HLLC with the minmod limiter.

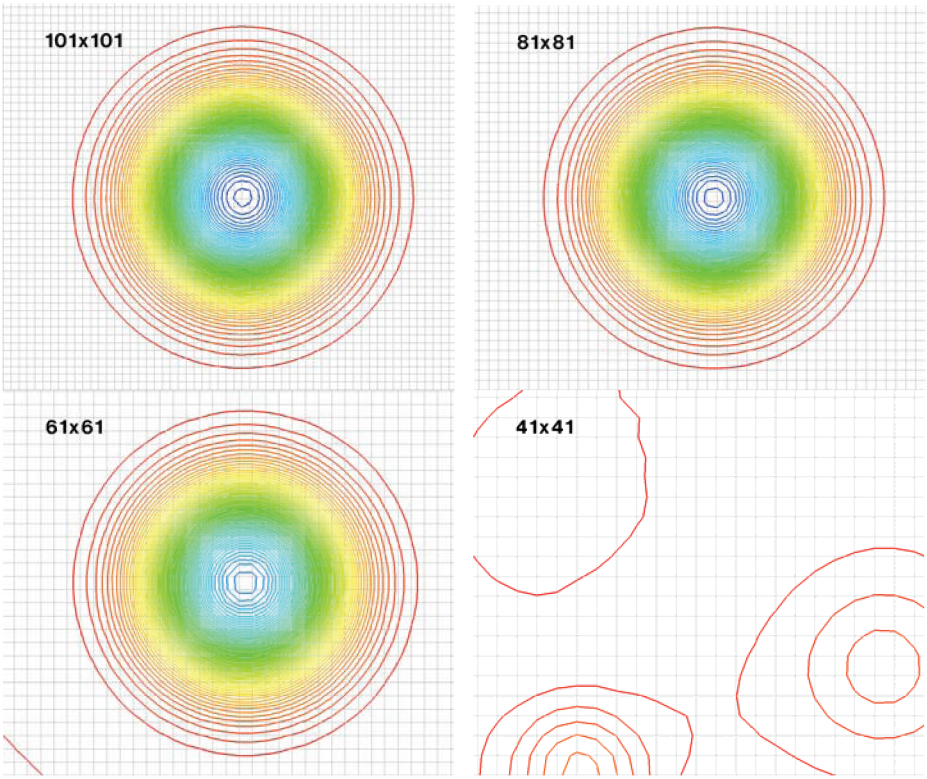

Fig. 5 Pressure contours for the convecting vortex after 100 passes through the grid using the fifth-order HLLC with WENOM.

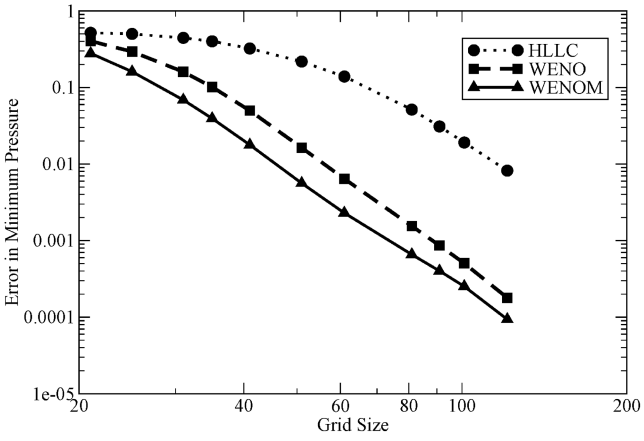

Fig. 6 Error in density after five passes through the grid.

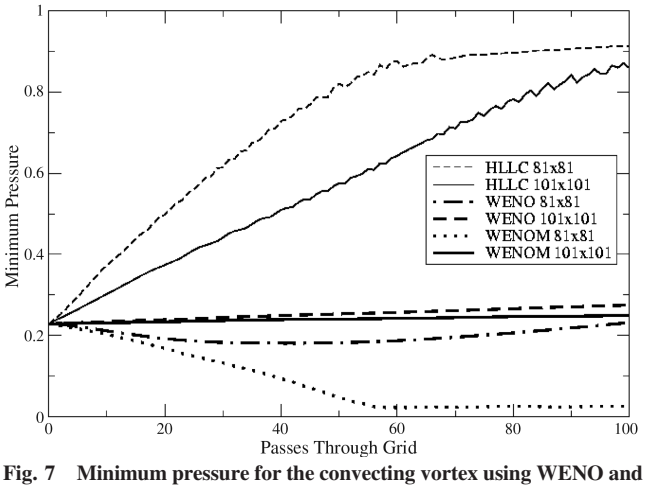

Fig. 7 Minimum pressure for the convecting vortex using WENO and WENOM showing skewed grid effect.

Two skewed grids (non-Cartesian) were generated with 81×81 and 101×101 grid points. The minimum pressure for both grids is shown in Fig. 7. The skewed grid causes the vortex to dissipate more rapidly than the Cartesian grid for both of the WENO algorithms. The third-order HLLC scheme is almost unaffected by the skewness of the grid and again shows excessive dissipation of the vortex. The vortex shows little dissipation for the 101×101 grid for WENO and WENOM. The WENO algorithm produces a reasonable solution for the 81×18 grid also. The WENOM algorithm produces a low pressure and density in the core of the vortex for the 81×18 grid. This nonphysical result can be seen in the pressure contours after 100 passes through the grid in Fig. 8.

The 81×81 uniform grid was decomposed into two grids: an 81×81 outer grid and an 61×61 inner grid. The center of the outer grid was blanked out and aligned (point-matched) interpolation boundaries were identified. Triple (TF), double (DF), and single (SF) fringe interpolations were evaluated. This simulation required the vortex to cross two interpolation boundaries for each cycle through the grid and is a stringent test of the overset boundary capability. Results are shown in Fig. 9. The triple fringe point aligned WENO and WENOM solutions are seen to agree with the single grid solutions shown in Fig. 4. Reducing to single or double fringe is seen to increase the dissipation of the vortex with WENO and WENOM. The WENO and WENOM double fringe solution is still much better than the third-order HLLC with double fringe.

A nonaligned 61×61 inner grid (points not coincident with the outer grid) with a triple fringe interpolation stencil is shown in Fig. 10. This grid system was used to evaluate whether the trilinear interpolation (second order in space) used in OVERFLOW 2 would be adequate for these higher order schemes. The triple fringe solution shown in Fig. 11 is seen to produce more dissipation of the vortex than the double fringe solution on the aligned grids for both WENO and WENOM shown in Fig. 8. Both of the WENO schemes still produce better results than the third-order HLLC scheme. This indicates that a higher order interpolation method [24] is required to maintain the high-order accuracy for the fifth-order schemes for nonaligned overlap boundaries.

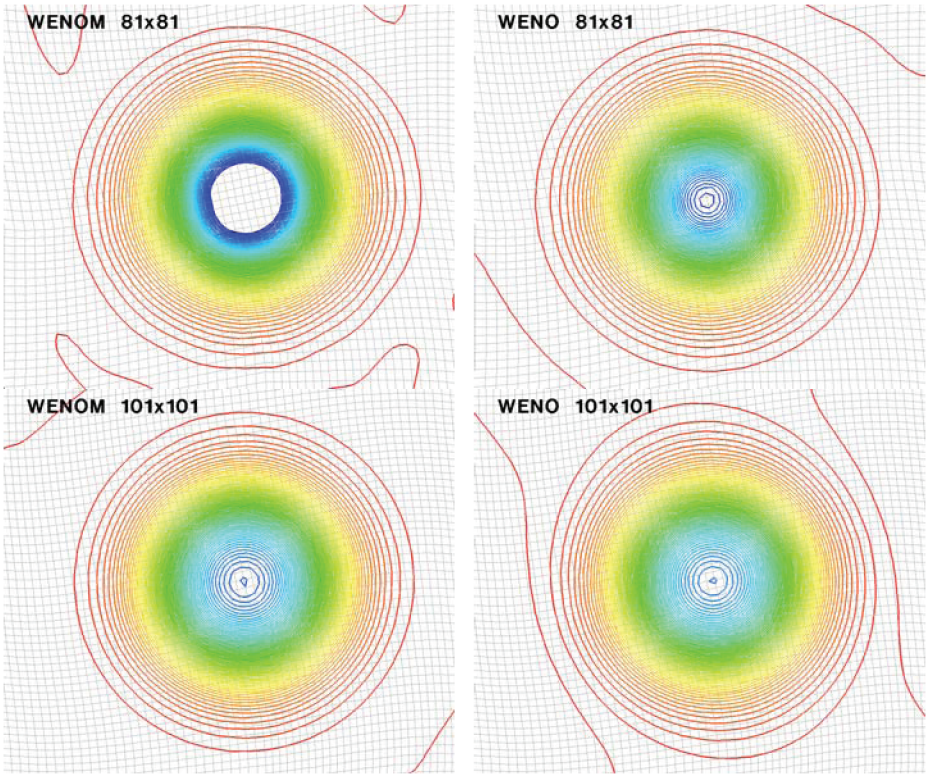

Fig. 8 Pressure contours after 100 passes through the grid for the skewed grids.

Hypersonic Cylinder Bow Shock

The hypersonic bow shock experimental data of Holden et al. [25] provide a good test of the ability of the numerical schemes to capture extremely strong shocks and to predict heat transfer at high speeds. The experiment was run at a freestream Mach number of 16.01, a Reynolds number (based on a cylinder diameter) of 9.11×10^4, a freestream temperature of 77.8°R, and a wall temperature of 540°R. The nitrogen test medium can still be considered a perfect gas at these conditions. The flow over the 3-in. diam cylinder is laminar for this case. The computational grid was 161×141 with a wall spacing corresponding to the y^+ value of 0.1. This case has a temperature ratio across the shock of about 50 and a pressure ratio across the shock of about 300.

The flowfield was initialized with a single time step at a freestream Mach number of 0.8. This transonic solution was then scaled to a freestream Mach number of 16.01. This provided a small region of subsonic flow at the nose of the cylinder so that the shock could form and push away from the body. Two levels of grid sequencing were used to set up the flowfield (299 iterations on the coarse level and 100 iterations on the midlevel). The case was run time accurately with a time step of 3.6×10^{-6} s. Five Newton subiterations were used at each time step with all of the inviscid flux algorithms.

The surface pressure coefficient is shown in Fig. 12. All of the flux schemes compare well with modified Newtonian theory. Predicted heat transfer is compared to data in Fig. 13. All three flux algorithms do an excellent job in predicting the magnitude of the heat transfer for this case. The L2 norm of the residuals is shown in Fig. 14a. All of the algorithms have a similar convergence behavior and plateau after about 850 time steps. Finally the drag coefficient convergence

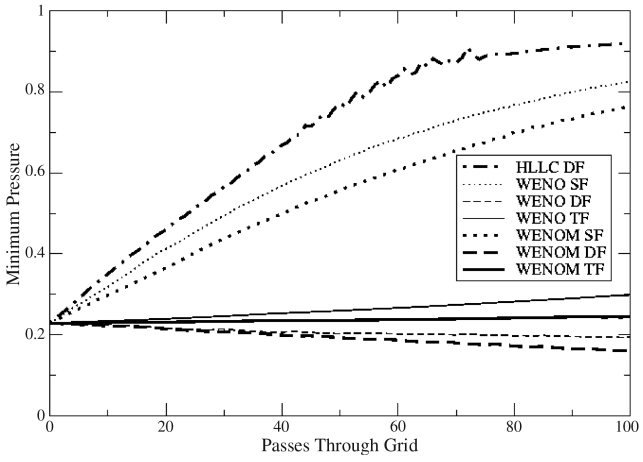

Fig. 9 Minimum pressure for the convecting vortex showing overset interpolation effects for point aligned grids.

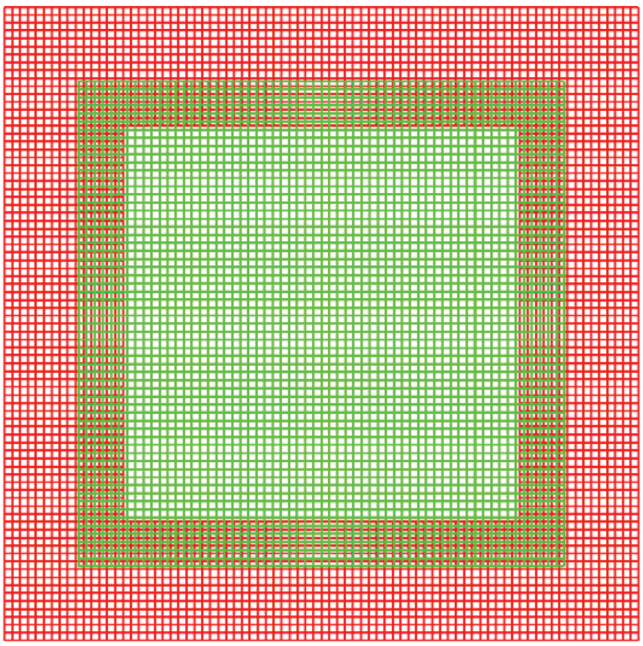

Fig. 10 Grid system for nonaligned overset computations for the convecting vortex.

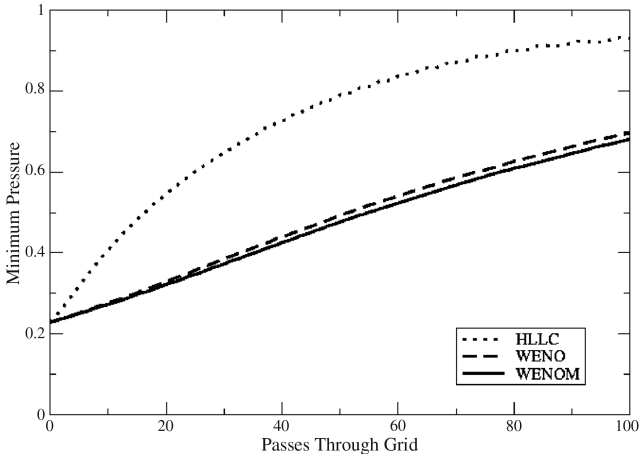

Fig. 11 Minimum pressure for the convecting vortex showing overset interpolation effects for point nonaligned grids.

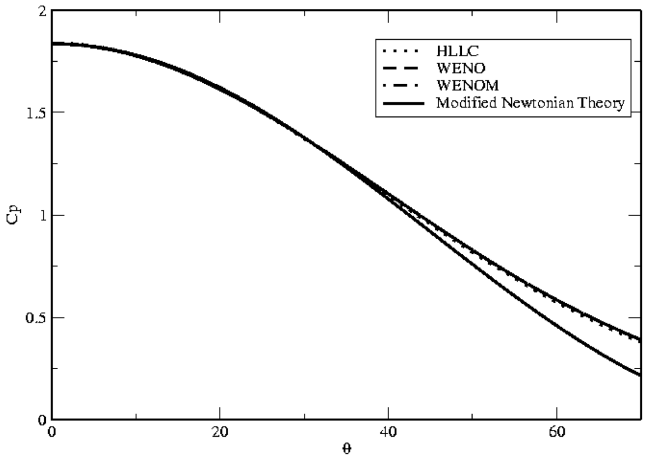

Fig. 12 Pressure coefficient for the Holden bow shock test case on the fine wall spacing grid.

history is shown in Fig. 14b. All of the flux schemes converge to the same drag coefficient after about 500 time steps.

Weapons Internal Carriage and Separation $L/D = 4.5$ Bay

Unsteady computations for the weapons internal carriage and separation (WICS) [26] $L/D = 4.5$ bay were performed for $M = 0.95$ and $Re = 2.5 \times 10^6$/ft. The weapons bay was 18 in. long, 4 in. wide, and 4 in. deep. The bay was located behind a 15-in. flat plate in the experimental configuration. The computational geometry was a

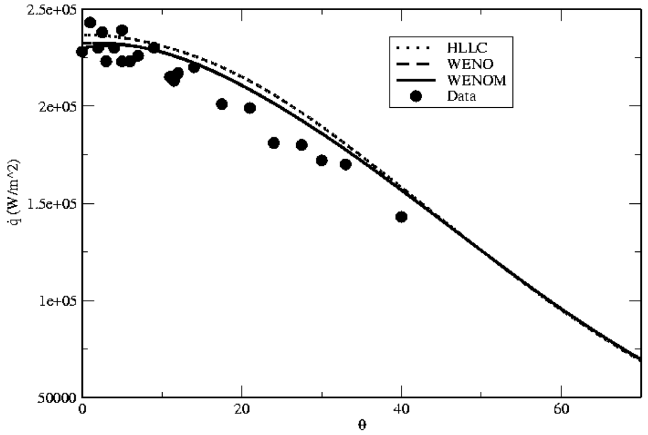

Fig. 13 Heat transfer for the Holden bow shock test case on the fine wall spacing grid.

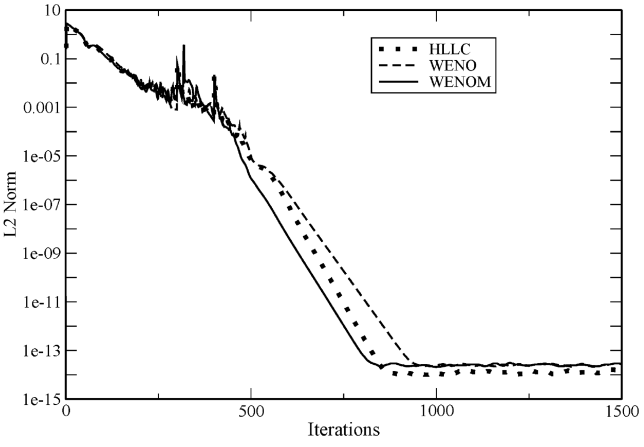

a)

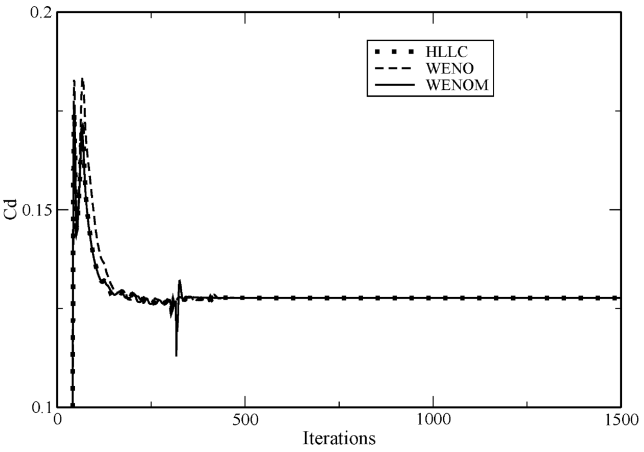

b)

Fig. 14 a) L2 norm of the residual for the Holden bow shock test case; b) drag coefficient convergence for the Holden bow shock test case.

flat plate that extended 15 in. upstream of the bay to match the experimental geometry and 25 in. downstream of the bay. The sides of the computational grid extended 50 in. on either side of the bay centerline. The full bay geometry was modeled using wall functions [27]. The entire computational grid had 1.5×10^6 points, and 3.2×10^5 points were used to discretize the bay. The wall spacing was chosen as 0.0075 in., which corresponds to a y^+ of 50 on the upstream plate. The wall spacing inside the bay was set to 0.075 in. The larger wall spacing may be used inside the bay because the wall shear stress is much lower there. The overset grid system was generated to provide triple fringe point aligned interpolation boundaries to maintain the fifth-order accuracy throughout the computational domain for the WENO and WENOM solutions. Double fringe point aligned interpolation boundaries were used for the third-order HLLC solution.

The Spalart–Allmaras detached eddy simulation [28] hybrid RANS/LES turbulence model was used in this study. The calculations were run 12,000 iterations and the final 8192 time steps were statistically analyzed. The equations were solved implicitly using the unfactored SSOR solver in OVERFLOW 2. A time accurate solution was obtained using second-order time differencing. Three Newton subiterations were used to locally converge the solution at each time step. All calculations were performed using the 1.6×10^{-5} s time step that was shown to be adequate for time accuracy in [29].

Time-averaged Mach number contours with velocity vectors are shown on the symmetry plane in Fig. 15 for the WENOM solutions. The time-averaged flow has a large vortex in the front half of the bay and a smaller vortex near the backwall. The location of the K12 and K18 pressure transducers are also shown in Fig. 16. The time-averaged pressure coefficient on the WICS bay ceiling and backwall

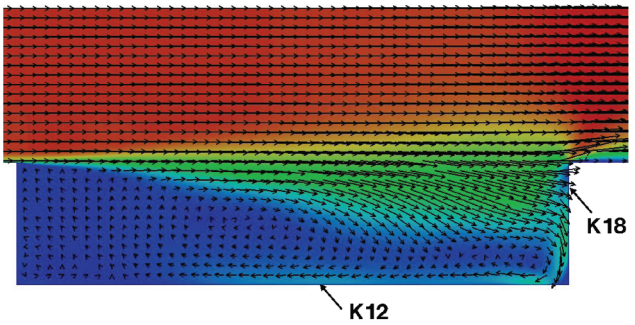

Fig. 15 Time-averaged Mach number contours on the WICS bay symmetry plane.

is shown in Fig. 16. Both of the fifth-order results are in better agreement with the data than the third-order solution. The overall sound pressure level (OASPL) on the ceiling and backwall is shown in Fig. 17. Again both the third- and fifth-order results are in reasonable agreement with the data. Spectral results for the K12 and K18 transducer locations are shown in Fig. 18. The K18 transducer is in a dynamic region of the flow because of its proximity to the shear layer above the bay. Seven data windows of 2048 samples were averaged to produce the spectra that are presented. The error [28] in the OASPL (defined as the difference of the individual window result and the averaged result divided by the averaged result) was less than 1%. Both the third- and fifth-order results are in good agreement with the data for the first two spectral peaks for the K18 location. The fifth-order result continues to predict the proper acoustic level throughout the entire measured frequency range while the third-order solution begins to roll off at about 1500 Hz for the K12 transducer. This improved frequency matching indicates that the fifth-order scheme is resolving much smaller turbulent scales than the third-order algorithm on the same computational grid.

Wing Tip Vortex

Laser-velocimeter measurements were made in the near-field region of the wing tip in [30]. The experimental setup is shown in Fig. 19 and consisted of a NACA 0012 wing with a rounded tip attached to a wind-tunnel wall. The wing had a 4 ft chord (Ch) and a 3 ft semispan (b). The freestream velocity was 170 ft/s, the angle of attack was 10 deg, and the Reynolds number based on the chord was 4×10^6.

The computational grid included the tunnel and the airfoil. An overset grid system of seven grids composed of 5.8×10^6 points was used in this study. The first point off the wall was set to $y^+ = 1$ on the wing and on the tunnel wall that supports the wing. Wall functions [25] were used for the other three tunnel walls and the first point off the wall was set to $y^+ = 50$. A triple fringe interpolation boundary was used to allow the full 7 point stencil for the WENO schemes to be maintained across interpolated computational boundaries. Traditional double fringe boundaries were used with the third-order HLLC scheme. A Cartesian grid was used in the tip vortex region to locally refine the grid system. This grid used the recommended spacings from [30] ($\Delta x = 0.01$Ch, $\Delta y = 0.005$Ch, and $\Delta z = 0.005$Ch) in the vortex region. A cross section of the grid in the tip region is shown in Fig. 20.

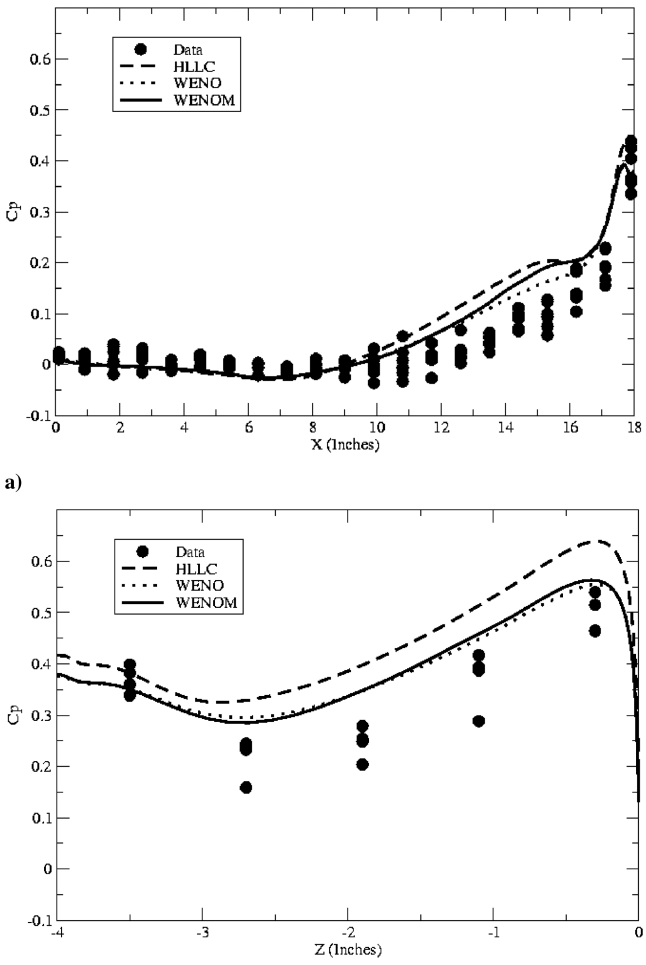

Fig. 16 a) Time-averaged pressure coefficient on the WICS bay ceiling; b) time-averaged pressure coefficient on the WICS bay backwall.

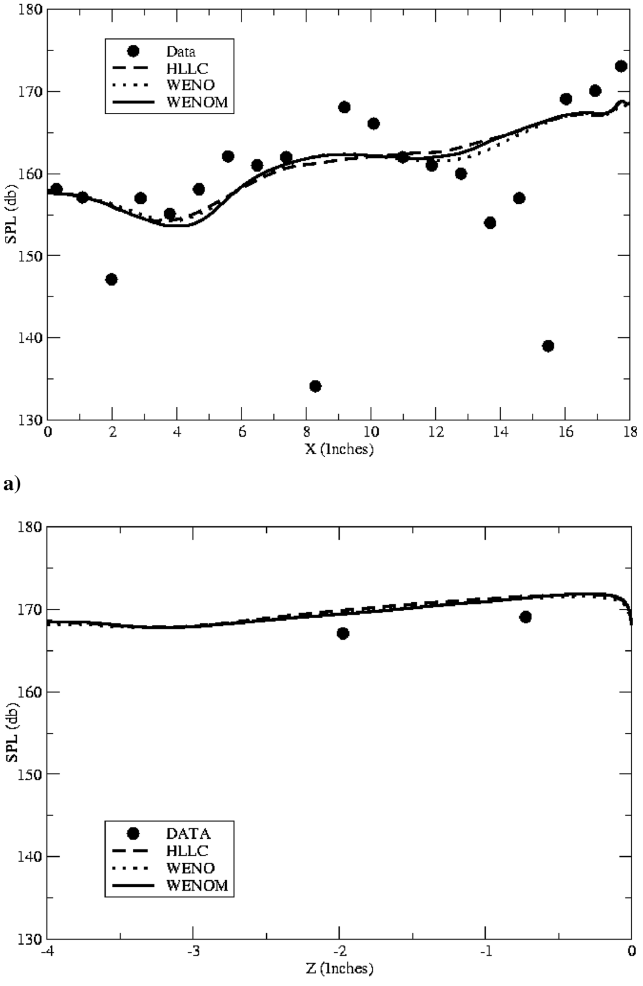

Fig. 17 a) Overall sound pressure level for the WICS bay ceiling; b) overall sound pressure level for the WICS bay backwall.

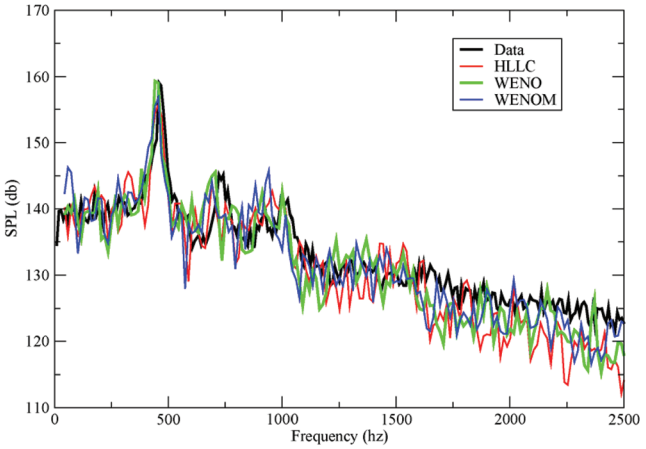

a)

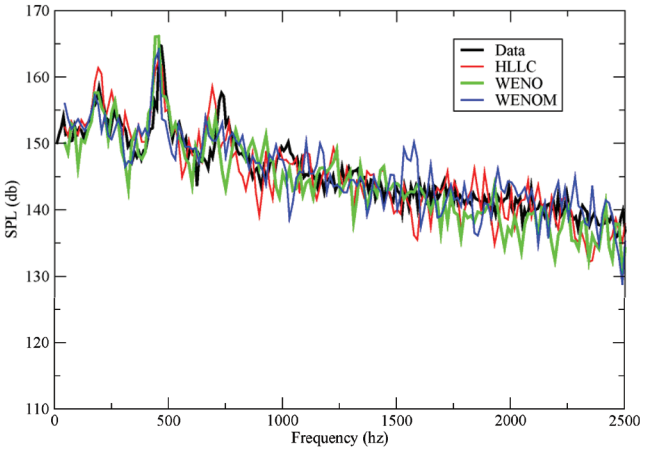

b)

Fig. 18 a) Sound pressure level spectrum for the K12 transducer location for the WICS bay; b) sound pressure level spectrum for the K18 transducer location for the WICS bay.

The baseline Baldwin–Barth turbulence model was found to provide too much eddy viscosity in the vortex core and overdamped the vortex in [30]. Both the Baldwin–Barth and the Spalart–Allmaras one-equation turbulence models use a turbulence production term of the form

$$P(\tilde{\nu}) = C_{b1}\tilde{\nu}\Omega \tag{27}$$

where C_{b1} is a constant, $\tilde{\nu}$ is the turbulence variable, and Ω is the vorticity magnitude. The vorticity reaches a local maximum in the core of a vortex, and hence the eddy viscosity increases rapidly. Dacles-Mariani et al. [30] suggested the production term be replaced

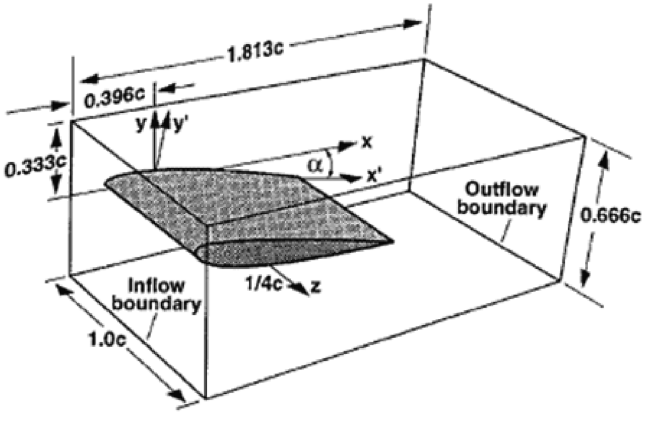

Fig. 19 Experimental geometry.

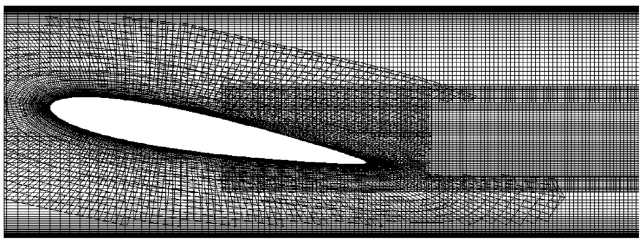

Fig. 20 Computational grid in the tip region.

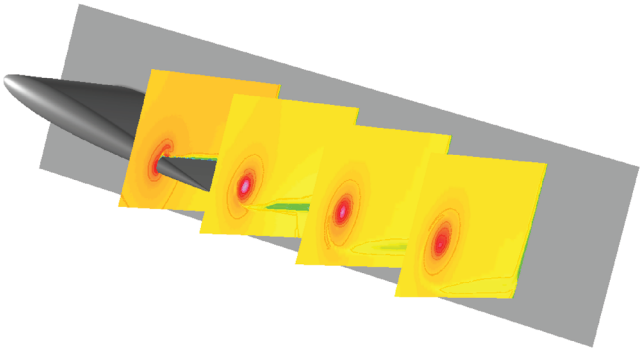

Fig. 21 Axial velocity contours.

by

$$P(\tilde{\nu}) = C_{b1}\tilde{\nu}[\Omega + C_{\text{vor}}\min(0, S_t - \Omega)] \tag{28}$$

where S_t is the magnitude of the strain. The strain goes to zero in the core of a vortex, so Eq. (28) converts the production term to a dissipation term in the vortex core if C_{vor} is greater than 1. Dacles-Mariani et al. [30] recommended $C_{\text{vor}} = 2$. Shur et al. [31] presented a similar rotation and curvature correction to the Spalart–Allmaras turbulence model that is also based on vorticity and strain rates. The Ref. [31] correction, designated as the Spalart–Allmaras rotation and curvature (SARC) model by the authors, was used in this study. The modified form of the production term has almost no effect in boundary layers and shear layers because the magnitude of the strain and the magnitude of the vorticity are almost equal for these flows and the correction term goes to zero.

The equations were solved implicitly using the unfactored SSOR solver. A time accurate solution was obtained using second-order time differencing. Three Newton subiterations were used to locally converge the solution at each time step. The time step was chosen to be 0.006 s. Low Mach number preconditioning was not used in this study. Solution convergence was judged based on the forces on the wing and normally required about 2500 iterations.

Axial velocity contours using the WENOM inviscid fluxes are shown in Fig. 21. A vorticity isosurface using the WENOM inviscid fluxes is shown in Fig. 22. The wing tip vortex is shown to be well defined and persistent in the near field.

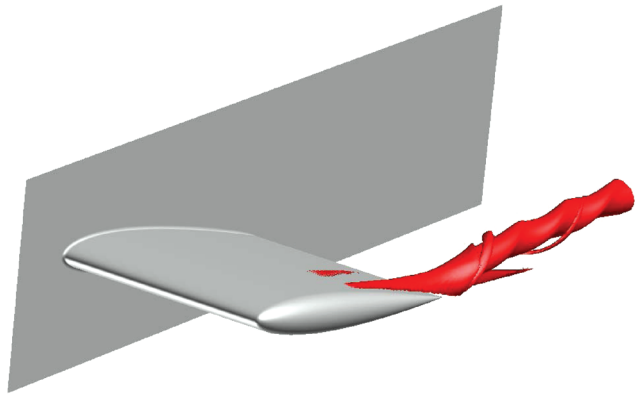

Fig. 22 Vorticity isosurface.

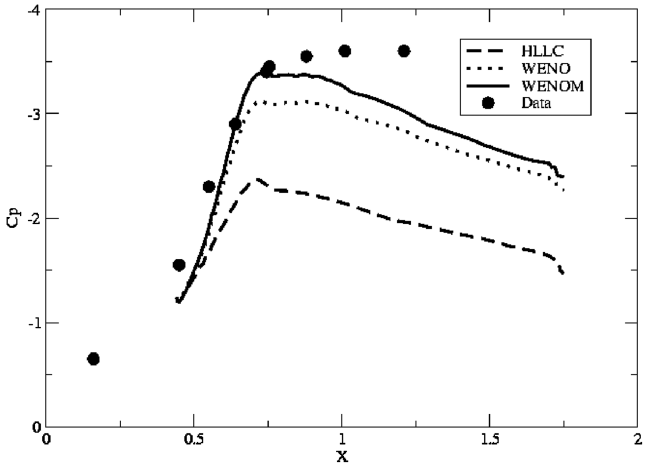

Fig. 23 Pressure coefficient in the vortex core.

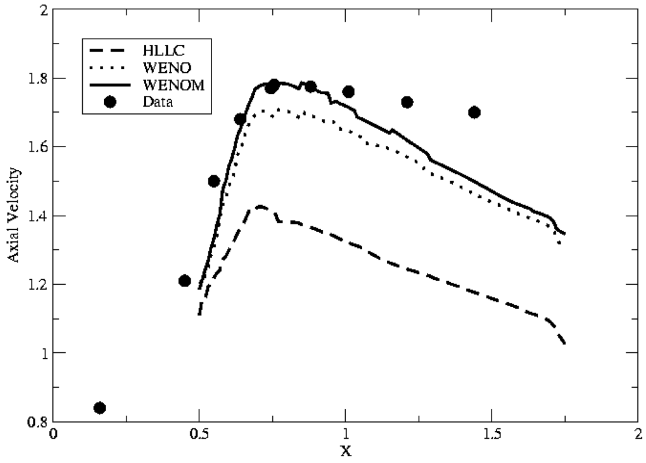

Fig. 24 Axial velocity in the vortex core.

The pressure coefficients and the axial velocity in the core of the vortex for each of the turbulence models and each of the flux algorithms are shown in Figs. 23 and 24 respectively. Both quantities are underpredicted using the HLLC flux algorithm, whereas both of the WENO schemes are in better agreement with the data. The tangential velocity at $x/\mathrm{Ch} = 1.2$ is shown in Fig. 25. Again the HLLC scheme has overdamped the vortex while both WENO schemes are in good agreement with the data. The current grid has 11 points across the viscous core of the vortex ($\bar{R}/\mathrm{Ch} < 0.03$).

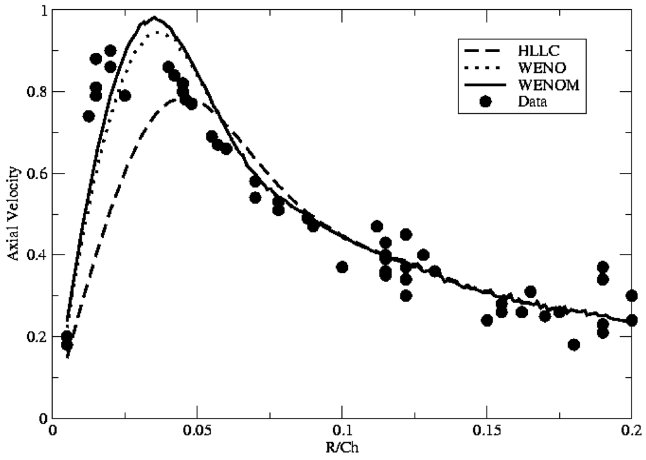

Fig. 25 Tangential velocity at $x/c = 1.2$.

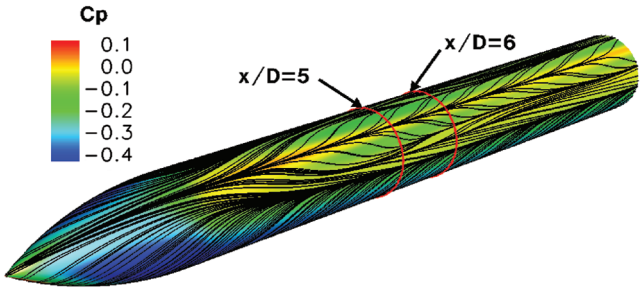

Fig. 26 Surface streak lines and pressure coefficient contours for the forebody.

Inclined Ogive Cylinder

The simulation of turbulent crossflow separation about slender bodies at high angle of attack has been challenging for computational fluid dynamics methods. Traditional RANS turbulence models produce excessive eddy viscosity in the core of the crossflow vortices and overdamp the solutions. The experimental data of Lamont [32] have been used to study this problem in [33,34]. The geometry consisted of a two diameter tangent-ogive nose mounted on a 6-in. diam cylindrical forebody. Surface pressure measurements were obtained on the body for a range of angles of attack and Reynolds numbers. The test condition used in the simulations conducted here was a freestream Mach number of 0.2, an angle of attack of 20 deg, and a Reynolds number based on a cylinder diameter of 4.0×10^6. Comparisons will be made to surface pressure data at $x/D = 5$ and 6.

A grid refinement study was conducted in [33]. The computational grid for the half-body used here had 151 points axially, 91 points circumferentially (2 deg increment), and 121 points in the normal direction. The wall spacing was 1.0×10^{-5} diameters ($y^+ = 2$) and the grid had 101 normal points in the boundary layer and vortex region. The grid used in this study is slightly finer than the grid independent fine mesh used in [33]. The time step was chosen to be $\Delta t = 0.114$ s. Low Mach number preconditioning was not used in this study. The SARC [31] turbulence model was used. Solution convergence was judged based on the forces on the forebody and normally required about 1000 iterations. All cases were run time accurately and all solutions achieved a steady-state solution.

Streak lines on the surface of the forebody are shown along with pressure coefficient contours in Fig. 26. The separation lines for the primary and secondary vortices are clearly evident. Vorticity magnitude contours at $x/D = 5$ and 6 are shown in Fig. 27 for the HLLC and WENOM flux algorithms using the SARC turbulence model. The vortex is resolved with about 11 points across the vortex for the WENOM algorithm at both locations. The HLLC algorithm produces lower peak vorticity at both locations than the WENOM algorithm. The surface pressure distributions for the HLLC and WENOM flux algorithms and for the SARC turbulence model are shown for $x/D = 5$ and $x/D = 6$ in Fig. 28. The experimental surface pressure measurements are consistently higher than the predictions on the windward side of the body. Similar trends have been seen in other studies including [32,33]. Degani et al. [34] noted that "... this is the result of the high-angle-of-attack flow condition, in which the windward flow was directed into the pressure taps." This causes the measured pressures on the windward side to be higher than the actual static pressure. The WENO and WENOM results are almost indistinguishable and provide better agreement with the data on the leeward side for both flux algorithms at both locations. The pressure coefficient in the vortex core is shown in Fig. 29. The WENO and WENOM algorithms are similar and predict a pressure coefficient magnitude that is about 50% higher than the HLLC algorithm.

Conclusions

Two fifth-order spatial WENO schemes for convected fluxes were evaluated in the OVERFLOW 2 code. The schemes improved solution quality over a third-order spatial HLLC scheme. The

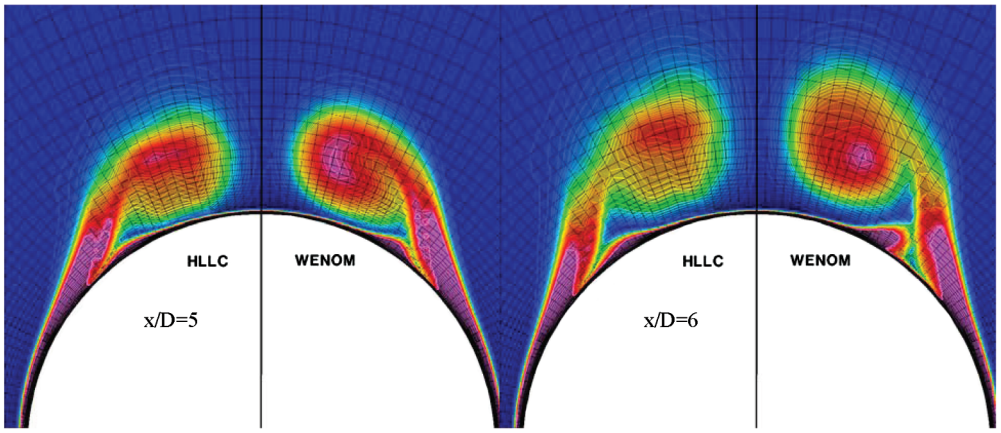

Fig. 27 Vorticity magnitude contours for the forebody with the SARC turbulence model.

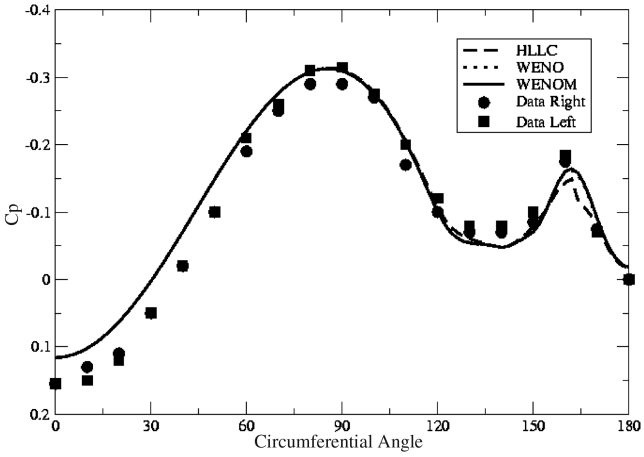

a)

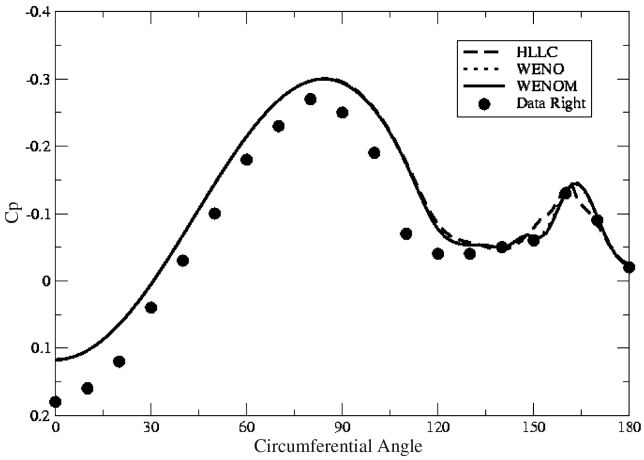

b)

Fig. 28 a) Pressure coefficient for the forebody with the SARC turbulence model at $x/D = 5$; b) pressure coefficient for the forebody with the SARC turbulence model at $x/D = 6$.

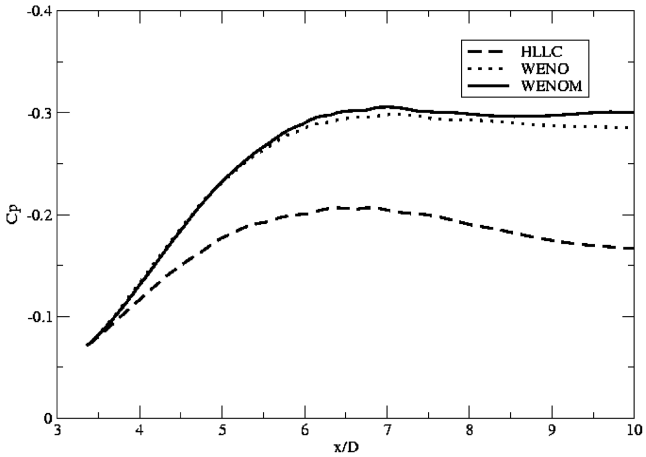

Fig. 29 Pressure coefficient in the vortex core for the forebody with the SARC turbulence model.

improved spatial resolution and reduced numerical dissipation allowed disturbances to be propagated for longer distances. Both WENO schemes were found to be as numerically stable as the extremely robust third-order spatial HLLC scheme. Both WENO schemes performed well in the presence of extremely strong shocks and for highly unsteady flow simulations.

The WENO scheme worked well on all combinations of grids tested here. The WENOM scheme produced better results than the WENO scheme on Cartesian grids, but produced an unphysical result on an underresolved smoothly skewed grid for the convected vortex case. Some form of correction for non-Cartesian grids is probably required for the WENOM scheme.

Both of the fifth-order spatial WENO schemes performed better than the third-order spatial HLLC scheme on the two three-dimensional problems examined here. The WENO schemes provided better agreement with data over a larger frequency range for the unsteady bay problem. The WENO schemes also provided much better agreement for the near-field wing tip vortex velocities and for the pressure coefficient on the tangent-ogive forebody using the same computational grid.

The WENO schemes and the triple fringe grid assembly routines have been included in the production release of OVERFLOW 2.1. The current trilinear interpolation used to generate the interpolated values at noninjected overlap points was shown to cause degradation in the order of accuracy of the solution for the vortex convection case. A higher order interpolation scheme is required to remove this error. This is left as an area for future work. Possible improvements from higher order viscous terms should also be investigated in the future.

Acknowledgments

The support of R. H. Nichols and R. W. Tramel by the U.S. Army Space and Missile Defense Command and by the Department of Defense (DoD) High Performance Computing Modernization Program (HPCMP) Productivity Enhancement and Technology Transfer (PET) is greatly appreciated.

References

[1] Visbal, M., and Gaitonde, D., "High-Order-Accurate Methods for Complex Unsteady Flows," *AIAA Journal*, Vol. 37, No. 10, 1999, pp. 1231–1239. doi:10.2514/2.591

[2] Rizzetta, D. P., and Visbal, M. R., "Large-Eddy Simulation of Supersonic Cavity Flowfields Including Flow Control," AIAA Paper 2002-2853, June 2002.

[3] Gordnier, R., Visbal, M., Gursul, I., and Wang, Z., "Computational and Experimental Investigation of a Nonslender Delta Wing," AIAA Paper 2007-894, Jan. 2007.

[4] Ladeinde, F., Alabi, K., Safta, C., Cai, X., and Johnson, F., "The First High-Order CFD Simulation of Aircraft: Challenges and Opportunities," AIAA Paper 2006-1526, Jan. 2006.

[5] Thomas, P., and Lombard, C., "Geometric Conservation Law and Its Application to Flow Computations on Moving Grids," *AIAA Journal*, Vol. 17, No. 10, 1979, pp. 1030–1037. doi:10.2514/3.61273

[6] Shu, C., and Osher, S., "Efficient Implementation of Essentially Non-Oscillatory Shock Capturing Schemes II (Two)," *Journal of Computational Physics*, Vol. 83, July 1989, pp. 32–78. doi:10.1016/0021-9991(89)90222-2

[7] Liu, X.-D., Osher, S., and Chan, T., "Weighted Essentially Nonoscillatory Schemes," *Journal of Computational Physics*, Vol. 115, Nov. 1994, pp. 200–212. doi:10.1006/jcph.1994.1187

[8] Jiang, G.-S., and Shu, C.-W., "Efficient Implementation of Weighted ENO Schemes," *Journal of Computational Physics*, Vol. 126, June 1996, pp. 202–228. doi:10.1006/jcph.1996.0130

[9] van Leer, B., "Towards the Ultimate Conservative Difference Scheme, V. A Second Order Sequel to Godunov's Method," *Journal of Computational Physics*, Vol. 32, July 1979, pp. 101–136. doi:10.1016/0021-9991(79)90145-1

[10] De Rango, S., and Zingg, D., "Higher-Order Spatial Discretization for Turbulent Aerodynamic Computations," *AIAA Journal*, Vol. 39, No. 7, 2001, pp. 1296–1304. doi:10.2514/2.1472

[11] Nichols, R., Tramel, R., and Buning, P., "Solver and Turbulence Model Upgrades to OVERFLOW 2 for Unsteady and High-Speed Applications," AIAA Paper 2006-2824, June 2006.

[12] Toro, E. F., Spruce, M., and Speares, W., "Restoration of the Contact Surface in the HLL Riemann Solver," *Shock Waves*, Vol. 4, No. 1, 1994, pp. 25–34. doi:10.1007/BF01414629

[13] Harten, A., Lax, P., and van Leer, B., "On Upstream Differencing and Godunov-Type Scheme for Hyperbolic Conservation Laws," *SIAM Review*, Vol. 25, No. 1, 1983, pp. 35–61. doi:10.1137/1025002

[14] Batten, P., Clarke, N., Lambert, C., and Causon, D., "On the Choice of Wavespeeds for the HLLC Riemann Solver," *SIAM Journal of Scientific Computations*, Vol. 18, No. 6, Nov. 1997, pp. 1553–1557.

[15] Einfeldt, B., "On Gudunov-Type Methods for Gas Dynamics," *SIAM Journal on Numerical Analysis*, Vol. 25, No. 2, April 1988, pp. 294–318. doi:10.1137/0725021

[16] Titarev, V., and Toro, E., "Finite-Volume WENO Schemes for Three-Dimensional Conservation Laws," *Journal of Computational Physics*, Vol. 201, Nov. 2004, pp. 238–260. doi:10.1016/j.jcp.2004.05.015

[17] Shen, Y., Wang, B., and Zha, G., "Implicit WENO Scheme and High Order Viscous Formulas for Compressible Flows," AIAA Paper 2007-4431, June 2007.

[18] Henrick, A., Aslam, T., and Powers, J., "Mapped Weighted Essentially Non-Oscillatory Schemes: Achieving Optimal Order Near Critical Points," *Journal of Computational Physics*, Vol. 207, Aug. 2005, pp. 542–567. doi:10.1016/j.jcp.2005.01.023

[19] Merriman, B., "Understanding the Shu–Osher Conservative Finite Difference Form," *Journal of Scientific Computing*, Vol. 19, Nos. 1–3, 2003, pp. 309–322. doi:10.1023/A:1025312210724

[20] Meakin, R., "The Chimera Method of Simulation for Unsteady Three-Dimensional Viscous Flow," *Computational Fluid Dynamics Review 1995*, edited by M. Hafez and K. Oshima, Wiley, New York, 1995, pp. 70–86.

[21] van Albada, G. D., van Leer, B., and Roberts, W., "A Comparative Study of Computational Methods in Cosmic Gas Dynamics," *Astronomy and Astrophysics*, Vol. 108, No. 1, April 1982, pp. 76–84.

[22] Pulliam, T. H., and Chaussee, D. S., "A Diagonalized Form of an Implicit Approximate Factorization Algorithm," *Journal of Computational Physics*, Vol. 39, Feb. 1981, pp. 347–363. doi:10.1016/0021-9991(81)90156-X

[23] Yee, H-C., Sandham, N., and Djomehri, M., "Low Dissipative High Order Shock-Capturing Methods Using Characteristic-Based Filters," *Journal of Computational Physics*, Vol. 150, March 1999, pp. 199–238. doi:10.1006/jcph.1998.6177

[24] Sherer, S. E., and Scott, J. N., "High-Order Compact Finite-Difference Methods on General Overset Grids," *Journal of Computational Physics*, Vol. 210, Dec. 2005, pp. 459–496. doi:10.1016/j.jcp.2005.04.017

[25] Holden, S. M., Kolly, J. M., and Martin, S. C., "Shock/Shock Interaction Heating in Laminar and Low-Density Hypersonic Flows," AIAA Paper 96-1866, June 1996.

[26] Dix, R. E., and Bauer, R. C., "Experimental and Theoretical Study of Cavity Acoustics," Arnold Engineering Development Center (AEDC) TR-99-4, May 2000.

[27] Nichols, R. H., and Nelson, C. C., "Wall Function Boundary Conditions Including Heat Transfer and Compressibility," *AIAA Journal*, Vol. 42, No. 6, 2004, pp. 1107–1114. doi:10.2514/1.3539

[28] Spalart, P., Jou, W.-H., Strelets, M., and Allmaras, S., "Comments on the Feasibility of LES for Wings and on a Hybrid RANS/LES Approach," *First AFOSR Conference on DNS/LES*, edited by C. Liu and Z. Liu, Greyden Press, Columbus, OH, Aug. 1997.

[29] Nichols, R. H., "Comparison of Hybrid RANS/LES Turbulence Models for a Circular Cylinder and a Generic Weapons Bay," *AIAA Journal*, Vol. 44, No. 6, 2006, pp. 1207–1219. doi:10.2514/1.17016

[30] Dacles-Mariani, J., Zilliac, G., Chow, J., and Bradshaw, P., "Numerical/Experimental Study of a Wingtip Vortex in the Near Field," *AIAA Journal*, Vol. 33, No. 9, 1995, pp. 1561–1568. doi:10.2514/3.12826

[31] Shur, M. L., Strelets, M. K., Travin, A. K., and Spalart, P. R., "Turbulence Modeling in Rotating and Curved Channels: Assessing the Spalart-Shur Correction," *AIAA Journal*, Vol. 38, No. 5, 2000, pp. 784–792. doi:10.2514/2.1058

[32] Lamont, P., "Pressures Around an Inclined Ogive Cylinder with Laminar, Transitional, or Turbulent Separation," *AIAA Journal*, Vol. 20, No. 11, 1982, pp. 1492–1499. doi:10.2514/3.51212

[33] Murman, S., "Vortex Filtering for Turbulence Models Applied to Crossflow Separation," AIAA Paper 2001-0114, Jan. 2001.

[34] Degani, D., Schiff, L., and Levy, Y., "Numerical Prediction of Subsonic Turbulent Flows over Slender Bodies at High Incidence," *AIAA Journal*, Vol. 29, No. 12, 1991, pp. 2054–2061. doi:10.2514/3.10841

Z. Wang
Associate Editor